

**DEVELOPMENT OF A ROTARY WING NAVIER-STOKES CFD CODE
BASED ON TLNS3D CODE**

**Final Report
of
the Grant DAAL03-92-G-0416**

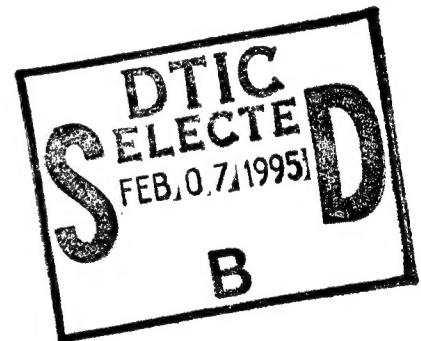
**for the period of
September 30, 1992 - August 31, 1994**

by

Hong Hu, Principal Investigator

**Hampton University
Hampton, Virginia 23668**

September 1994



**Prepared for
U.S. Army Research Office
P.O.Box 12211
Research Triangle Park, NC 27709**

**Approved for Public Release
Distribution Unlimited**

DTIC QUALITY INSPECTED 1

19950203 157

REPORT DOCUMENTATION PAGE			Form Approved OMB No. 0704-0188	
Public reporting burden for this collection of information is estimated to average 1 hour per response, including the time for reviewing instructions, searching existing data sources, gathering and maintaining the data needed, and completing and reviewing the collection of information. Send comments regarding this burden estimate or any other aspect of this collection of information, including suggestions for reducing this burden, to Washington Headquarters Services, Directorate for Information Operations and Reports, 1215 Jefferson Davis Highway, Suite 1204, Arlington, VA 22202-4302, and to the Office of Management and Budget, Paperwork Reduction Project (0704-0188), Washington, DC 20503.				
1. AGENCY USE ONLY (Leave blank)	2. REPORT DATE September 1994	3. REPORT TYPE AND DATES COVERED Final 30 Sept 92 - 31 Aug 94		
4. TITLE AND SUBTITLE DEVELOPMENT OF A ROTARY WING NAVIER-STOKES CFD CODE BASED ON TLNS3D CODE		5. FUNDING NUMBERS DAA03-92-G-0416		
6. AUTHOR(S) Hong Hu				
7. PERFORMING ORGANIZATION NAME(S) AND ADDRESS(ES) Hampton University Hampton, Virginia 23668		8. PERFORMING ORGANIZATION REPORT NUMBER		
9. SPONSORING / MONITORING AGENCY NAME(S) AND ADDRESS(ES) U.S. Army Research Office P. O. Box 12211 Research Triangle Park, NC 27709-2211		10. SPONSORING / MONITORING AGENCY REPORT NUMBER ARO 30697.1-EG-H		
11. SUPPLEMENTARY NOTES The view, opinions and/or findings contained in this report are those of the author(s) and should not be construed as an official Department of the Army position, policy, or decision, unless so designated by other documentation.				
12a. DISTRIBUTION / AVAILABILITY STATEMENT Approved for public release; distribution unlimited.			12b. DISTRIBUTION CODE	
13. ABSTRACT (Maximum 200 words) This report documents the development of a multi-grid Navier-Stokes code for rotary wing calculations, TLNS3DR. The TLNS3DR is based on the fixed-wing TLNS3D code by adding a rotation term and making necessary modifications on boundary conditions. The TLNS3D code solves the thin-layer Navier-Stokes equations using an explicit multistage Runge-Kutta type of time stepping with multigrid method. The TLNS3DR code re-formulates the TLNS3D code in the rotor blade-fixed moving frame of reference and solves relative motion of fluids. In this report, the formulation of the Navier-Stokes equations in the moving frame of reference in terms of relative velocity is given. Several numerical examples are then presented. The results of rotor blade in hover calculated by the new TLNS3DR code seems quantitatively correct. The computation also shows that this multigrid code is efficient.				
14. SUBJECT TERMS Rotor-blade in hover, Navier-Stokes equations, moving frame of reference, relative motion, tip vortex, multigrid method, multi-stage Runge-Kutta time stepping			15. NUMBER OF PAGES 38	
			16. PRICE CODE	
17. SECURITY CLASSIFICATION OF REPORT UNCLASSIFIED	18. SECURITY CLASSIFICATION OF THIS PAGE UNCLASSIFIED	19. SECURITY CLASSIFICATION OF ABSTRACT UNCLASSIFIED	20. LIMITATION OF ABSTRACT UL	

FOREWORD

The research reported in this document was performed under the grant, DAAL03-92-G-0416, from the U.S. Army Research Office. Dr. T. L. Doligalski was the technical monitor. Drs. H. Jones, F. Caradonna and Y. Yu were Scientific Liaison Representatives on this project. Dr. H. Jones has provided helpful suggestions and guidance during this investigation. The TLNS3D code and WTCO code were provided by Dr. V. N. Vatsa of NASA- LaRC, and his assistance is truly appreciated.

Accession For	
NTIS GRA&I	<input checked="checked" type="checkbox"/>
DTIC TAB	<input type="checkbox"/>
Unannounced	<input type="checkbox"/>
Justification	
By	
Distribution	
Availability Codes	
Dist	Avail and/or Special
A-1	

TABLE OF CONTENTS

	Page
FOREWORD	i
TABLE OF CONTENTS	ii
LIST OF FIGURES	iii
SUMMARY	1
1. INTRODUCTION	2
2. THE NAVIER-STOKES EQUATIONS	2
3. NUMERICAL SCHEME	7
4. NUMERICAL EXAMPLES	9
5. CONCLUDING REMARKS	10
REFERENCES	11
FIGURES	13
LIST OF PUBLICATIONS	31
LIST OF PARTICIPATING SCIENTIFIC PERSONNEL	32
REPORT OF INVENTIONS	33

LIST OF FIGURES

	Page
Figure 1. Frames of reference	13
Figure 2. C-O mesh	14
Figure 3a. Non-rotating subsonic flow, pressure coefficient	15
Figure 3b. Non-rotating subsonic flow, local Mach number	16
Figure 3c. Subsonic flow in hover, pressure coefficient	17
Figure 3d. Subsonic flow in hover, local Mach number	18
Figure 3e. Non-rotating subsonic flow, residual	19
Figure 3f. Subsonic flow in hover, residual	20
Figure 4a. Non-rotating transonic flow, pressure coefficient	21
Figure 4b. Non-rotating transonic flow, local Mach number	22
Figure 4c. Transonic flow in hover, pressure coefficient	23
Figure 4d. Transonic flow in hover, local Mach number	24
Figure 4e. Non-rotating transonic flow, residual	25
Figure 4f. Transonic flow in hover, residual	26
Figure 5a. Lifting transonic flow in hover, pressure coefficient	27
Figure 5b. Lifting transonic flow in hover, local Mach number	28
Figure 5c. Lifting transonic flow in hover, tip flow field investigation	29
Figure 5d. Lifting transonic flow in hover, residual	30

DEVELOPMENT OF A ROTARY WING NAVIER-STOKES CFD CODE BASED ON TLNS3D CODE

**Hong Hu
Hampton University
Hampton, Virginia 23668**

SUMMARY

This report documents the development of a multi-grid Navier-Stokes code for rotary wing calculations, TLNS3DR. The TLNS3DR is based on the fixed-wing TLNS3D code by adding a rotation term and making necessary modifications on boundary conditions. The TLNS3D code solves the thin-layer Navier-Stokes equations using an explicit multi-stage Runge-Kutta type of time stepping with multigrid method. The TLNS3DR code re-formulates the TLNS3D code in the rotor blade-fixed moving frame of reference and solves relative motion of fluids.

In this report, the formulation of the Navier-Stokes equations in the moving frame of reference in terms of relative velocity is given. Several numerical examples are then presented. The results of rotor blade in hover calculated by the new TLNS3DR code seems quantitatively correct. The computation also shows that this multigrid code is efficient.

1. INTRODUCTION

The accurate and efficient calculation of rotor flow fields poses a particularly challenging problem in the computational helicopter aerodynamics community. The accurate calculation of the aerodynamic forces on the rotor requires a correct prediction of the vortex wake, including the blade trailing wake as well as the interaction of the tip vortex of one rotor blade with the following rotor blade. The generation of the free-wake and its interaction with the blade make the helicopter aerodynamic computation extremely complex.

The computational methods for calculating helicopter rotor flow fields can be divided into two types: integral equation methods (panel methods) and finite-difference/finite-volume methods. Integral equation methods for both incompressible and compressible rotor flows are developed by several investigators¹⁻⁵. The methods are able to treat rotor blade and vortex wake accurately and efficiently. However, they are restricted to linear, low-speed, subsonic, or at most, to nonlinear flows with weak shocks. This is a very serious limitation, because modern rotor blades operate in the transonic regime, where the nonlinear compressibility is important and the strong shocks can exist in the flow field. Finite-difference/finite-volume methods based on the full-potential^{6,7}, Euler⁸⁻¹⁰ and Navier-Stokes^{9,10} (NS) equations with a single grid for rotor flow fields are developed during the past few years, while more recently the calculations are mainly concerned with various NS equations. These methods, particularly NS including thin-layer NS methods, can treat compressible flows with shocks, including strong shocks, in the region of the rotor blade accurately. The effects of free-wake are captured fairly accurately as a part of the overall flowfield. However, the calculation of NS equations on a fine, single grid is expensive.

On the other hand, a multigrid NS Computational Fluid Dynamics (CFD) computer code, TLNS3D, is developed¹¹ for the fixed-wing motion. The TLNS3D code solves the thin-layer Navier-Stokes equations using an explicit multistage Runge-Kutta type of time-stepping with multigrid method. The philosophy of multigrid method is the use of successively coarser grids to compute corrections to a fine grid solution. The use of multigrid strategy results in a much faster convergence than single-grid method. The efficiency of the multigrid method using five-stage Runge-Kutta time-stepping is demonstrated¹¹ through computations for transonic flows over fixed wings. The code is shown to result in a significant reduction in CPU time as compared to the single-grid multistage time-stepping method.

The purpose of the present work is to develop a rotary-wing multigrid Navier-Stokes code, TLNS3DR, by modifying the TLNS3D code. The new code re-formulates the TLNS3D code in the rotor blade-fixed moving frame of reference and solves relative motion of fluids. In this report, the formulation of the Navier-Stokes equations in the moving frame of reference in terms of relative velocity is given. Several numerical examples are then presented. The results of rotor blade in hover calculated by the new TLNS3DR code seems quantitatively correct. The computation also shows that this multigrid code is efficient.

2. THE NAVIER-STOKES EQUATIONS

2.1 NS Equations in Space-fixed Frame of Reference

The basic equations under consideration are unsteady Navier-Stokes equations. In the space-fixed frame of reference, the dimensional form of the NS equations in the conservative form is given by

$$\frac{\partial \rho^*}{\partial t^*} + \nabla^* \cdot (\rho^* \vec{V}^*) = 0 \quad (1)$$

$$\frac{\partial}{\partial t^*}(\rho^* \vec{V}^*) + \nabla^* \cdot (\rho^* \vec{V}^* \vec{V}^* + p^* \bar{I}) - \nabla^* \cdot \bar{\tau}^* = 0 \quad (2)$$

$$\frac{\partial}{\partial t^*}(\rho^* e^*) + \nabla^* \cdot (\rho^* h^* \vec{V}^*) - \nabla^* \cdot (\bar{\tau}^* \cdot \vec{V}^* - \vec{q}^*) = 0 \quad (3)$$

with

$$p^* = \rho^*(\gamma - 1)(e^* - \frac{V^{*2}}{2}) \quad (4)$$

$$h^* = \frac{\gamma p^*}{(\gamma - 1)\rho^*} + \frac{V^{*2}}{2} \quad (5)$$

where ρ^* is the density, \vec{V}^* the velocity vector, t^* the time, p^* the pressure, \bar{I} the identity matrix tensor, $\bar{\tau}^*$ the viscous shear stress tensor, e^* the total energy given by $e^* = e_i^* + V^{*2}/2$ with e_i^* as internal energy, h^* the total enthalpy, and \vec{q}^* the heat conduction given by $\vec{q}^* = -k\nabla^* T^*$ where T^* is the temperature. The superscript, *, denotes dimensional quantities.

Using the free-stream density (ρ_∞^*), the free-stream speed of sound divided by the square-root of the gas specific heat ratio ($a_\infty^*/\sqrt{\gamma}$), and wing root-chord length (c), the above equations take the following form:

$$\frac{\partial \rho}{\partial t} + \nabla \cdot (\rho \vec{V}) = 0 \quad (6)$$

$$\frac{\partial}{\partial t}(\rho \vec{V}) + \nabla \cdot (\rho \vec{V} \vec{V} + p \bar{I}) - \nabla \cdot \bar{\tau} = 0 \quad (7)$$

$$\frac{\partial}{\partial t}(\rho e) + \nabla \cdot (\rho h \vec{V}) - \nabla \cdot (\bar{\tau} \cdot \vec{V} - \vec{q}) = 0 \quad (8)$$

with

$$p = \rho(\gamma - 1)(e - \frac{V^2}{2}) \quad (9)$$

$$h = \frac{\gamma p}{(\gamma - 1)\rho} + \frac{V^2}{2} \quad (10)$$

where $\rho = \rho^*/\rho_\infty^*$; $\nabla = c\nabla^*$; $\vec{V} = \vec{V}^* \sqrt{\gamma}/a_\infty^*$; $t = t^* a_\infty^*/(c\sqrt{\gamma})$; $p = p^* \gamma / \rho_\infty^* a_\infty^{*2} = p^*/p_\infty^*$; $\bar{\tau} = \bar{\tau}^*/p_\infty^*$; $e = e^* \gamma / a_\infty^{*2}$; $h = h^* \gamma / a_\infty^{*2}$; $\vec{q} = \vec{q}^* \gamma \sqrt{\gamma} / (\rho_\infty^* a_\infty^{*2} a_\infty^*)$; and the subscript, ∞ , refers to free-stream condition.

Equations (6), (7) and (8) along with Eqs. (9) and (10) are Navier-Stokes equations in non-dimensional form, where $\bar{\tau}$ and \bar{q} are given by

$$\bar{\tau} = \frac{M_\infty \sqrt{\gamma} \mu}{R_e} \left[\left(\frac{\partial u_i}{\partial x_j} + \frac{\partial u_j}{\partial x_i} \right) - \frac{2}{3} \delta_{i,j} \frac{\partial u_k}{\partial x_k} \right] \quad (11)$$

and

$$\bar{q} = (q_x, q_y, q_z) = - \frac{\mu M_\infty \gamma \sqrt{\gamma}}{R_e P_r (\gamma - 1)} \nabla T \quad (12)$$

respectively, where μ is the non-dimensional viscous coefficient given by $\mu = \mu^*/\mu_\infty^* = T^{3/2}(1+C)/(T+C)$, and $C = 0.4317$; T is the non-dimensional temperature given by $T = T^*/T_\infty^*$; R_e is the Reynolds number given by $R_e = \rho_\infty^* V_\infty^* c / \mu_\infty^*$; M_∞ is the free-stream Mach number given by $M_\infty = V_\infty^* / a_\infty^*$; and P_r is the Prandtl number given by $P_r = c_p \mu_\infty^* / k_\infty^*$ with c_p as gas specific heat and k_∞^* as free-stream conductivity.

2.2 NS Equations in Blade-fixed Frame of Reference

For a general motion of a rotor blade, the governing equations are simple to solve if a rotor blade-fixed moving frame of reference formulation is used. In addition to the space-fixed frame of reference $OXYZ$, a blade-fixed moving frame of reference $oxyz$ is introduced as shown in Figure 1. The moving frame of reference $oxyz$ is translating at a velocity of $\vec{V}_o(t)$ and rotating around a pivot point (rotor blade axis: $\vec{r}_p(x_p, y_p, z_p)$) at an angular velocity of $\vec{\Omega}(t)$. The relation for the non-dimensional absolute velocity ($\vec{V} = (u, v, w)$), relative velocity ($\vec{V}_r = (u_r, v_r, w_r)$) and transformation velocity ($\vec{V}_t = (u_t, v_t, w_t) = \vec{V}_o + \vec{V}_e = \vec{V}_o + \vec{\Omega} \times \vec{r}$) is given by

$$\vec{V} = \vec{V}_r + \vec{V}_o + \vec{\Omega} \times \vec{r} \quad (13)$$

where \vec{r} is the position vector measured in the blade-fixed moving frame of reference relative to \vec{r}_p . It should be noted that the transformation velocity (\vec{V}_t) includes both translation (\vec{V}_o) and rotation ($\vec{\Omega} \times \vec{r}$) velocities and therefore this formulation is general for both hovering and forwarding motion of the helicopter.

To express Eqs. (6), (7) and (8) in terms of the blade-fixed moving frame of reference, the relations of substantial and local derivatives are used:

$$\frac{Db}{Dt} = \frac{D'b}{Dt'} \quad (14)$$

$$\frac{\partial b}{\partial t} = \frac{\partial' b}{\partial t'} - \vec{V}_t \cdot \nabla b \quad (15)$$

$$\frac{D\vec{B}}{Dt} = \frac{D'\vec{B}}{Dt'} + \vec{\Omega} \times \vec{B} \quad (16)$$

$$\frac{\partial \vec{B}}{\partial t} = \frac{\partial' \vec{B}}{\partial t'} - \vec{V}_t \cdot \nabla \vec{B} + \vec{\Omega} \times \vec{B} \quad (17)$$

where the prime (') denotes the operation with respect to the blade-fixed moving frame of reference; b is a scalar and \vec{B} is a vector.

By using Eqs. (13) through (17), Eqs.(6), (7) and (8) become

$$\frac{\partial' \rho}{\partial t'} + \nabla \cdot (\rho \vec{V}_r) = 0 \quad (18)$$

$$\frac{\partial'}{\partial t'}(\rho \vec{V}_r) + \nabla \cdot (\rho \vec{V}_r \vec{V}_r + p \vec{I}) - \nabla \cdot \vec{\tau}_r = -\rho \vec{a}_t \quad (19)$$

$$\begin{aligned} & \frac{\partial'}{\partial t'}(\rho e_r) + \nabla \cdot (\rho h_r \vec{V}_r) - \nabla \cdot (\vec{\tau}_r \cdot \vec{V}_r - \vec{q}) \\ &= -\rho[\vec{V}_r \cdot \vec{a}_o + (\vec{\Omega} \times \vec{r}) \cdot \vec{a}_o + \vec{V}_o \cdot (\vec{a}_t - \vec{\Omega} \times \vec{V}_r) \\ &+ \vec{V}_r \cdot (\frac{\partial' \vec{\Omega}}{\partial t'} \times \vec{r}) + (\vec{\Omega} \times \vec{r}) \cdot (\frac{\partial' \vec{\Omega}}{\partial t'} \times \vec{r})] \end{aligned} \quad (20)$$

with

$$p = (\gamma - 1)\rho(e_r - \frac{V_r^2}{2} + \frac{V_t^2}{2}) \quad (21)$$

$$h_r = \frac{\gamma p}{\rho(\gamma - 1)} + \frac{V_r^2}{2} - \frac{V_t^2}{2} \quad (22)$$

$$\begin{aligned} \vec{a}_t &= (a_{tx}, a_{ty}, a_{tz}) = \frac{D\vec{V}}{Dt} - \frac{D'\vec{V}_r}{Dt'} \\ &= \vec{a}_o + (\frac{\partial' \vec{\Omega}}{\partial t'} \times \vec{r}) + 2(\vec{\Omega} \times \vec{V}_r) + \vec{\Omega} \times (\vec{\Omega} \times \vec{r}) \end{aligned} \quad (23)$$

$$\vec{\tau}_r = \frac{M_\infty \sqrt{\gamma} \mu}{Re} [(\frac{\partial u_{ri}}{\partial x_j} + \frac{\partial u_{rj}}{\partial x_i}) - \frac{2}{3} \delta_{i,j} \frac{\partial u_{rk}}{\partial x_k}] \quad (24)$$

where \vec{a}_o is the acceleration of the translation velocity given by $\vec{a}_o = D\vec{V}_o/Dt$ and h_r is the total rothalpy. Equations (18), (19) and (20) along with Eqs. (21) through (24) are set of Navier-Stokes equations in the moving frame of reference in terms of relative velocity.

In the cartesian coordinates, Eqs. (18), (19) and (20) are rewritten in the matrix form as:

$$\frac{\partial' \hat{U}_r}{\partial t'} + \frac{\partial}{\partial x}(\hat{F}_r - \hat{F}_{vr}) + \frac{\partial}{\partial y}(\hat{G}_r - \hat{G}_{vr}) + \frac{\partial}{\partial z}(\hat{H}_r - \hat{H}_{vr}) = \hat{S} \quad (25)$$

with

$$\hat{U}_r = [\rho, \rho u_r, \rho v_r, \rho w_r, \rho e_r]^t \quad (26)$$

$$\hat{F}_r = [\rho u_r, \rho u_r^2 + p, \rho u_r v_r, \rho u_r w_r, \rho u_r h_r]^t \quad (27)$$

$$\hat{G}_r = [\rho v_r, \rho v_r u_r, \rho v_r^2 + p, \rho v_r w_r, \rho v_r h_r]^t \quad (28)$$

$$\hat{H}_r = [\rho w_r, \rho w_r u_r, \rho w_r v_r, \rho w_r^2 + p, \rho w_r h_r]^t \quad (29)$$

$$\hat{F}_{vr} = [0, \tau_{rxx}, \tau_{rxy}, \tau_{rxz}, u_r \tau_{rxx} + v_r \tau_{rxy} + w_r \tau_{rxz} - q_x]^t \quad (30)$$

$$\hat{G}_{vr} = [0, \tau_{ryx}, \tau_{ryy}, \tau_{ryz}, u_r \tau_{ryx} + v_r \tau_{ryy} + w_r \tau_{ryz} - q_y]^t \quad (31)$$

$$\hat{H}_{vr} = [0, \tau_{rxx}, \tau_{rxy}, \tau_{rxz}, u_r \tau_{rxx} + v_r \tau_{rxy} + w_r \tau_{rxz} - q_z]^t \quad (32)$$

$$\begin{aligned} \hat{S} = & [0, -\rho a_{tx}, -\rho a_{ty}, -\rho a_{tz}, \\ & -\rho [\vec{V}_r \cdot \vec{a}_o + (\vec{\Omega} \times \vec{r}) \cdot \vec{a}_o + \vec{V}_o \cdot (\vec{a}_t - \vec{\Omega} \times \vec{V}_r) \\ & + \vec{V}_r \cdot (\frac{\partial' \vec{\Omega}}{\partial t'} \times \vec{r}) + (\vec{\Omega} \times \vec{r}) \cdot (\frac{\partial' \vec{\Omega}}{\partial t'} \times \vec{r})]]^t \end{aligned} \quad (33)$$

where \hat{U}_r is the field vector; \hat{F}_r , \hat{G}_r and \hat{H}_r are inviscid flux vectors; \hat{F}_{vr} , \hat{G}_{vr} and \hat{H}_{vr} are viscous flux vectors; and \hat{S} is the source vector due to the motion of the moving frame of reference. All field and flux vectors and viscous shear stresses are based on the relative velocity field. The subscript, r , denotes relative quantity.

2.3 NS Equations in Computational Domain

The Navier-Stokes equations given by Eq. (25) are then specialized to a body fitted coordinate system (ξ, η, ζ) in computational domain, where ξ , η and ζ represent the streamwise, normal and spanwise directions, respectively. The thin-layer assumption is employed by keeping viscous diffusion term in the normal (η) direction only, since the dominant viscous effects arise from viscous diffusion normal to the body surface for high-Reynolds-number turbulent flows. For the time-independent (ξ, η, ζ) coordinate system in the blade-fixed moving frame of reference, Eq. (25) becomes

$$\frac{\partial'}{\partial t'}(J^{-1}\hat{U}_r) + \frac{\partial F_r}{\partial \xi} + \frac{\partial G_r}{\partial \eta} + \frac{\partial H_r}{\partial \zeta} = \frac{\partial G_{vr}}{\partial \eta} + J^{-1}\hat{S} \quad (34)$$

with

$$\begin{aligned} F_r = & J^{-1}(\xi_x \hat{F}_r + \xi_y \hat{G}_r + \xi_z \hat{H}_r) \\ = & J^{-1}[\rho \tilde{u}_r, \rho \tilde{u}_r u_r + \xi_x p, \rho \tilde{u}_r v_r + \xi_y p, \rho \tilde{u}_r w_r + \xi_z p, \rho \tilde{u}_r h_r]^t \end{aligned} \quad (35)$$

$$\begin{aligned} G_r = & J^{-1}(\eta_x \hat{F}_r + \eta_y \hat{G}_r + \eta_z \hat{H}_r) \\ = & J^{-1}[\rho \tilde{v}_r, \rho \tilde{v}_r u_r + \eta_x p, \rho \tilde{v}_r v_r + \eta_y p, \rho \tilde{v}_r w_r + \eta_z p, \rho \tilde{v}_r h_r]^t \end{aligned} \quad (36)$$

$$\begin{aligned} H_r = & J^{-1}(\zeta_x \hat{F}_r + \zeta_y \hat{G}_r + \zeta_z \hat{H}_r) \\ = & J^{-1}[\rho \tilde{w}_r, \rho \tilde{w}_r u_r + \zeta_x p, \rho \tilde{w}_r v_r + \zeta_y p, \rho \tilde{w}_r w_r + \zeta_z p, \rho \tilde{w}_r h_r]^t \end{aligned} \quad (37)$$

$$\begin{aligned} G_{vr} = & J^{-1}(\eta_x \hat{F}_{vr} + \eta_y \hat{G}_{vr} + \eta_z \hat{H}_{vr}) \\ = & J^{-1} \frac{\sqrt{\gamma} M_\infty \mu \bar{e}}{Re} [0, \phi_1 u_{r\eta} + \eta_x \phi_2, \phi_1 v_{r\eta} + \eta_y \phi_2, \phi_1 w_{r\eta} + \eta_z \phi_2, \phi_1 a + \tilde{v}_r \phi_2]^t \end{aligned} \quad (38)$$

where

$$\tilde{u}_r = \xi_x u_r + \xi_y v_r + \xi_z w_r \quad (39)$$

$$\tilde{v}_r = \eta_x u_r + \eta_y v_r + \eta_z w_r \quad (40)$$

$$\tilde{w}_r = \zeta_x u_r + \zeta_y v_r + \zeta_z w_r \quad (41)$$

$$\phi_1 = \eta_x^2 + \eta_y^2 + \eta_z^2 \quad (42)$$

$$\phi_2 = \frac{1}{3}(\eta_x u_{r\eta} + \eta_y v_{r\eta} + \eta_z w_{r\eta}) \quad (43)$$

$$a = \left(\frac{q^2}{2}\right)_\eta + \left(\frac{\gamma}{\gamma - 1}\right) \frac{\tilde{\epsilon}}{P_r \bar{\epsilon}} T_\eta \quad (44)$$

$$q^2 = u_r^2 + v_r^2 + w_r^2 \quad (45)$$

and J^{-1} is the inverse Jacobian of the transformation. It should be noted that the viscosity (μ) and conductivity (k) are replaced by $\mu\bar{\epsilon}$ and $k\tilde{\epsilon}$, respectively, to include the effect of turbulence, where $\bar{\epsilon}$ is turbulence edge viscosity and $\tilde{\epsilon}$ is turbulence edge conductivity. The turbulence model used here is the algebraic model of Baldwin and Lomax¹².

Equation (34) is the most general form of thin-layer NS equations in the blade-fixed moving frame of reference in terms of relative velocity. The \hat{S} -term in Eq. (34) is the source term contributed from the time-dependent rotation ($\vec{\Omega}(t)$) and translation ($\vec{V}_o(t)$) of the rotor blade. For hovering motion which is the case considered here, and where $\vec{V}_o = 0$ and $\vec{\Omega} = 0\vec{i} - \Omega\vec{j} + 0\vec{k}$ with $\Omega = \text{constant}$, the \hat{S} -term in Eq. (34), or Eq. (33), reduces to

$$\hat{S} = \rho[0, (x - x_p)\Omega^2 + 2\Omega w_r, 0, (z - z_p)\Omega^2 - 2\Omega u_r, 0]^t \quad (46)$$

where (x_p, y_p, z_p) is the blade rotation axis as mentioned earlier.

3. NUMERICAL SCHEME

The present work is based on the fixed-wing TLNS3D code¹¹. The difference of the present NS formulation from the fixed-wing NS formulation of TLNS3D code is due to the source term, \hat{S} . Hence the numerical scheme follows exactly the one of the TLNS3D code with the addition of the source term (\hat{S}) into the code, along with the necessary modification of the boundary conditions.

3.1 Finite-Volume Discretization

Replacing the spatial derivatives by central differences in Eq. (34), the following semi-discrete form is obtained:

$$\begin{aligned} & \frac{\partial'}{\partial t'} (J^{-1} \hat{U}_r)_{i,j,k} + (F_{r,i+1/2,j,k} - F_{r,i-1/2,j,k}) \\ & + (G_{r,i,j+1/2,k} - G_{r,i,j-1/2,k}) \\ & + (H_{r,i,j,k+1/2} - H_{r,i,j,k-1/2}) \\ & = (G_{vri,j+1/2,k} - G_{vri,j-1/2,k}) + J_{i,j,k}^{-1} \hat{S}_{i,j,k} \end{aligned} \quad (47)$$

where

$$F_{ri\pm 1/2,j,k} = \frac{1}{2}(F_{ri,j,k} + F_{ri\pm 1,j,k}) \quad (48)$$

$$G_{ri,j\pm 1/2,k} = \frac{1}{2}(G_{ri,j,k} + G_{ri,j\pm 1,k}) \quad (49)$$

$$H_{ri,j,k\pm 1/2} = \frac{1}{2}(H_{ri,j,k} + H_{ri,j,k\pm 1}) \quad (50)$$

and $\Delta\xi$, $\Delta\eta$ and $\Delta\zeta$ are taken to be one. The cell centroidal point is (i, j, k) , and the half-integer subscripts refer to cell interface. The viscous term ($G_{vri,j\pm 1,k}$) is evaluated according to TLNS3D code using relative velocity. Artificial dissipation of TLNS3D code is used where the velocity is replaced by the relative velocity.

Using the notation Q_r to represent all inviscid flux terms, Q_{vr} to represent the viscous flux terms and D_r to represent the artificial dissipative fluxes for convenience, Eq. (47) is rewritten as

$$\frac{\partial'}{\partial t'}(J^{-1}\hat{U}_r)_{i,j,k} + Q_r = Q_{vr} + D_r + J_{i,j,k}^{-1}\hat{S}_{i,j,k} \quad (51)$$

where

$$\begin{aligned} Q_r = & (F_{ri+1/2,j,k} - F_{ri-1/2,j,k}) \\ & + (G_{ri,j+1/2,k} - G_{ri,j-1/2,k}) \\ & + (H_{ri,j,k+1/2} - H_{ri,j,k-1/2}) \end{aligned} \quad (52)$$

and

$$Q_{vr} = (G_{vri,j+1/2,k} - G_{vri,j-1/2,k}) \quad (53)$$

3.2 Multi-stage Time-Stepping Scheme

The source term (\hat{S}) is added into the five-stage Runge-Kutta time-stepping scheme used in the TLNS3D code. This time-stepping scheme is described as follows:

$$\begin{aligned} \hat{U}_r^{(0)} &= \hat{U}_r^{(n)} \\ \hat{U}_r^{(1)} &= \hat{U}_r^{(0)} - \alpha_1 \frac{\Delta t}{J-1} [Q_r^{(0)} + \beta_1 Q_{vr}^{(0)} - \gamma_1 D_r^{(0)} - J^{-1}\hat{S}] \\ \hat{U}_r^{(2)} &= \hat{U}_r^{(0)} - \alpha_2 \frac{\Delta t}{J-1} [Q_r^{(1)} + \beta_2 Q_{vr}^{(1)} - \gamma_1 D_r^{(0)} - \gamma_2 D_r^{(1)} - J^{-1}\hat{S}] \\ \hat{U}_r^{(3)} &= \hat{U}_r^{(0)} - \alpha_3 \frac{\Delta t}{J-1} [Q_r^{(2)} + \beta_3 Q_{vr}^{(2)} - \gamma_1 D_r^{(0)} - \gamma_2 D_r^{(1)} - \gamma_3 D_r^{(2)} - J^{-1}\hat{S}] \\ \hat{U}_r^{(4)} &= \hat{U}_r^{(0)} - \alpha_4 \frac{\Delta t}{J-1} [Q_r^{(3)} + \beta_4 Q_{vr}^{(3)} - \gamma_1 D_r^{(0)} - \gamma_2 D_r^{(1)} - \gamma_3 D_r^{(2)} - \gamma_4 D_r^{(3)} - J^{-1}\hat{S}] \\ \hat{U}_r^{(5)} &= \hat{U}_r^{(0)} - \alpha_5 \frac{\Delta t}{J-1} [Q_r^{(4)} + \beta_5 Q_{vr}^{(4)} - \gamma_1 D_r^{(0)} - \gamma_2 D_r^{(1)} - \gamma_3 D_r^{(2)} - \gamma_4 D_r^{(3)} - \gamma_5 D_r^{(4)} \\ &\quad - J^{-1}\hat{S}] \\ \hat{U}_r^{(n+1)} &= \hat{U}_r^{(5)} \end{aligned} \quad (54)$$

where the superscripts, (n) and $(n + 1)$, refer to time levels; and the superscripts, (0) through (5) , refer to multistage level within each time step. In addition to the five-stage time-stepping scheme, the local time-stepping and residual smoothing techniques are applied to accelerate the convergence of the scheme to steady state for rotor hovering motion. The details of the residual smoothing is discussed in Ref. [11].

3.3 Multigrid Acceleration Technique

The multigrid scheme of TLNS3D is employed for hovering motion calculations. The idea of multigrid is the use of successively coarser grids to compute corrections to a fine grid solution. The use of multigrid technique can significantly accelerate the convergence rate. In order to provide optimum damping of the high frequency errors, the coefficients of $\alpha_1 = 1/4, \alpha_2 = 1/6, \alpha_3 = 3/8, \alpha_4 = 1/2, \alpha_5 = 1, \beta_1 = 1, \beta_2 = 0, \beta_3 = 1, \beta_4 = 0, \beta_5 = 1$, and $\gamma_1 = 1, \gamma_2 = 0, \gamma_3 = 0.56, \gamma_4 = 0, \gamma_5 = 0.44$ are used according to TLNS3D. The coefficients on the residual smoothing are also carefully selected. The results presented in this report are obtained using a V-cycle multigrid scheme.

3.4 Boundary Conditions and Grid

A C-O type grid is employed. The grid is generated using the WTCO¹¹ code. Figure 2 is the partial view of C-O grid for the half-span rectangle rotor blade. A mesh consisting of $129 \times 65 \times 65$ points in the streamwise, spanwise and normal directions, respectively, is used.

On the blade surface, no-slip and no-penetration conditions are used by setting relative velocity (\vec{V}_r) to zero. The adiabatic wall condition and zero-normal pressure gradient condition at the wall are also applied at the blade surface. The farfield boundaries are treated by using Riemann invariants condition used in TLNS3D code¹¹. At the inboard-plane, near the rotation axis of the blade, the condition of $u_r/w_r = u_t/w_t = -(z - z_p)/(x - x_p)$ is used to guarantee that the radial velocity is zero at this boundary.

4. NUMERICAL EXAMPLES

Calculations are performed for a straight, untapered and untwisted rectangle blade with constant NACA0012 section. A single isolated blade is considered. The blade length is 12, while the chord length is 1. Flows at three different conditions for hovering motion are calculated: non-lifting shock-free subsonic flow, non-lifting transonic flow and lifting transonic flow. For the non-lifting flows, the calculations for fixed-wing motion under equivalent condition are also made for serving as reference solutions. Additional extensive calculations are made on the BERP blade, the UH-60A blade and a equivalent rectangle blade, and results are presented in Ref. [13].

The first example is for non-lifting shock-free subsonic flow. Figures 3a and 3b are the surface pressure and local Mach contours, respectively, for fixed-wing flow at $M_\infty = 0.628$ and $Re = 3.7 \times 10^6$. All Mach contours presented here are calculated at $j = 33$ which is about just outside the boundary layer. Figures 3c and 3d are the surface and local Mach contours, respectively, for hovering motion at $M_{tip} = 0.628$ and $Re = 3.7 \times 10^6$. By comparing the results of hovering motion with those of fixed-wing motion, it is seen that effects of rotation term, which is $J^{-1}\hat{S}$ in NS equations, are quantitatively correctly calculated. The solution for hovering motion looks reasonably correct. Figures 3e and 3f

are convergence history in terms of residual for fixed-wing motion and hovering motion, respectively. A total of 400 equivalent fine grid time steps (beased on the equivalent CPU time required) are used in both cases. The CPU time on the NASA-LaRC's CRAY-YMP with a single processor for all cases presented here is around 6100 seconds, which is about 0.011 seconds per fine grid point, or 27.98×10^{-6} seconds per fine grid point per time step.

The second example is for non-lifting transonic flow. Figures 4a and 4b are the surface pressure and local Mach contours, respectively, for fixed-wing flow at $M_\infty = 0.84$ and $Re = 4.97 \times 10^6$. Figures 4c and 4d are the surface and local Mach contours, respectively, for hovering motion at $M_{tip} = 0.84$ and $Re = 4.97 \times 10^6$. By comparing the results of hovering motion with those of fixed-wing motion, it is seen that effects of rotation term are quantitatively correctly calculated for this transonic flow case. The solution for hovering motion looks reasonably correct, where shock occurs in the tip region of the blade. Figures 4e and 4f are convergence history in terms of residual for fixed-wing motion and hovering motion, respectively. These two figures tell us that the solution for hovering motion does not converge as fast as one for fixed-wing motion, and this fact may due to the unsteadiness of the hovering motion.

The third numerical example is for lifting transonic flow. Figures 5a and 5b are the surface and local Mach contours, respectively, for hovering motion at angle-of-attack of 4.2° , $M_{tip} = 0.877$ and $Re = 3.93 \times 10^6$. The solution looks reasonably correct, where shock occurs in the tip region of the blade with a reasonable shock strength and location. Figure 5c is the tip cross flow vector field where the relative velocity is plotted. From this figure, it is seen that the tip roll-up vortex is captured with the current ($129 \times 65 \times 65$) mesh size, and the solution of the tip vortex looks quantitatively correct. Figures 5d is convergence history in terms of residual.

5. CONCLUDING REMARKS

The TLNS3D code is modified into TLNS3DR code for rotary-wing calculations. The solutions for helicopter rotor blade in hover are obtained using the new TLNS3DR code and the solutions, including shock and tip roll-up vortex, looks quantitatively correct. The accuracy of the new code is going to be tested, and the fine-tune of the code may be necessary to improve quality of the code. The application of multigrid method in the present rotary-wing calculations shows that the method is very efficient compared with the single grid method, although the solution for hovering motion converges slower than that for fixed-wing motion. The code's capability of capturing free tip vortex is promising as a analysis tool in rotor tip design.

REFERENCES

1. Landgrebe, A. J., "An Analytical and Experimental Investigation of Helicopter Rotor Hover Performance and Wake Geometry Characteristics," U.S. Army Air Mobility Research and Development Laboratories, Moffett Field, CA, USAAMRDL TR-71-24, June 1971.
2. Kocurek, J. D. and Tangler, J. L., "A Prescribed Wake Lifting Surface Hover Performance Analysis," *Journal of the American Helicopter Society*, Vol. 22, Jan. 1977, pp. 24-35.
3. Morino, L. and Bharadvaj, B. K., "Two Methods for Viscous and Inviscid Free-Wake Analysis of Helicopter Rotors," CCAD-TR-85-04-R, Boston University, 1985.
4. Felker, F. F., Quackenbush, T. R., Bliss, D. R. and Light, J. S., "Comparisons of Predicted and Measured Rotor Performance in Hover using a New Free-Wake Analysis," The 44th Annual Forum of the American Helicopter Society, Washington, DC, June 16018, 1988.
5. Hsu, A. T. and Wu, J. C., "Vortex Flow Model for the Blade-Vortex Interaction Problem," *AIAA Journal*, Vol. 26, No.5, May 1988, pp. 621- 623.
6. Caradonna, F. X., Desopper, A. and Tung, C., "Finite-Difference Modeling of Rotor Flows Including Wake Effects," The 8th European Rotorcraft Forum, Aix-Provence, France, Paper 2.7, Aug. 1982.
7. Egolf, T. A. and Sparks, S. P., "Hovering Rotor Airload Prediction Using a Full Potential Flow Analysis with Realistic Wake Geometry," The 41st Annual Forum of the American Helicopter Society, Ft. Worth, TX, May 1985.
8. Aggarwal, R. and Deese, J., "Euler Calculation for Flow Field of a Helicopter Rotor in Hover," AIAA 4th Applied Aerodynamics Conference, San Diego, CA, June 1986.
9. Sankar, N. L., Wake, B. E., Ruo, S. Y. and Malone, J. B., "Numerical Solution of Unsteady Rotational Flow Past Fixed and Rotary Wing Configurations," NASA CP-3022, 1989, pp. 351-374.
10. Srinivasan, G. R., Baeder, J. D., Obayashi, S. and McCroskey, W. J., "Flowfield of a Lifting Hovering Rotor - A Navier-Stokes Simulation," NASA TM - 102862.
11. Vatsa, V. N. and Wedan, B. W., "Development of a Multigrid Code for 3D Navier-Stokes Equations and Its Application to a Grid-refinement Study," *Computers & Fluids*, Vol. 18, No. 4, 1990, pp. 391-403.
12. Baldwin, B. S. and Lomax, H., "Thin Layer Approximation and Algebraic Model for Separated Turbulent Flows," AIAA Paper 78-0257, 1978.
13. Hu, H., "Application of Multigrid Computational Fluid Dynamics (CFD) Method To Rotor Design", DAAJ02-93-C-0021, Technical Report, U.S. Army Aviation Applied

Technology Directorate, December 1994.

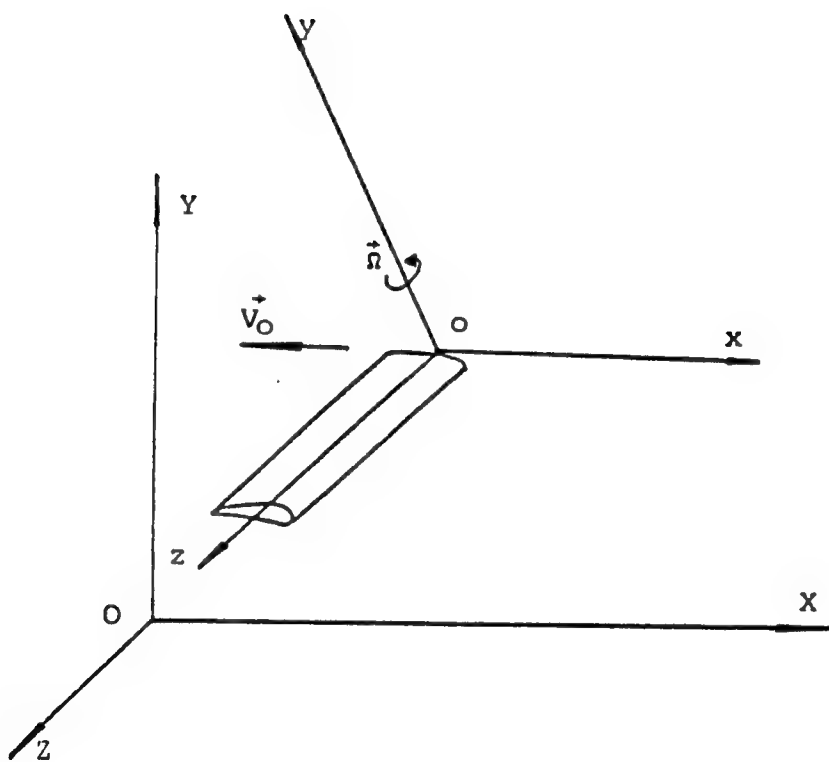
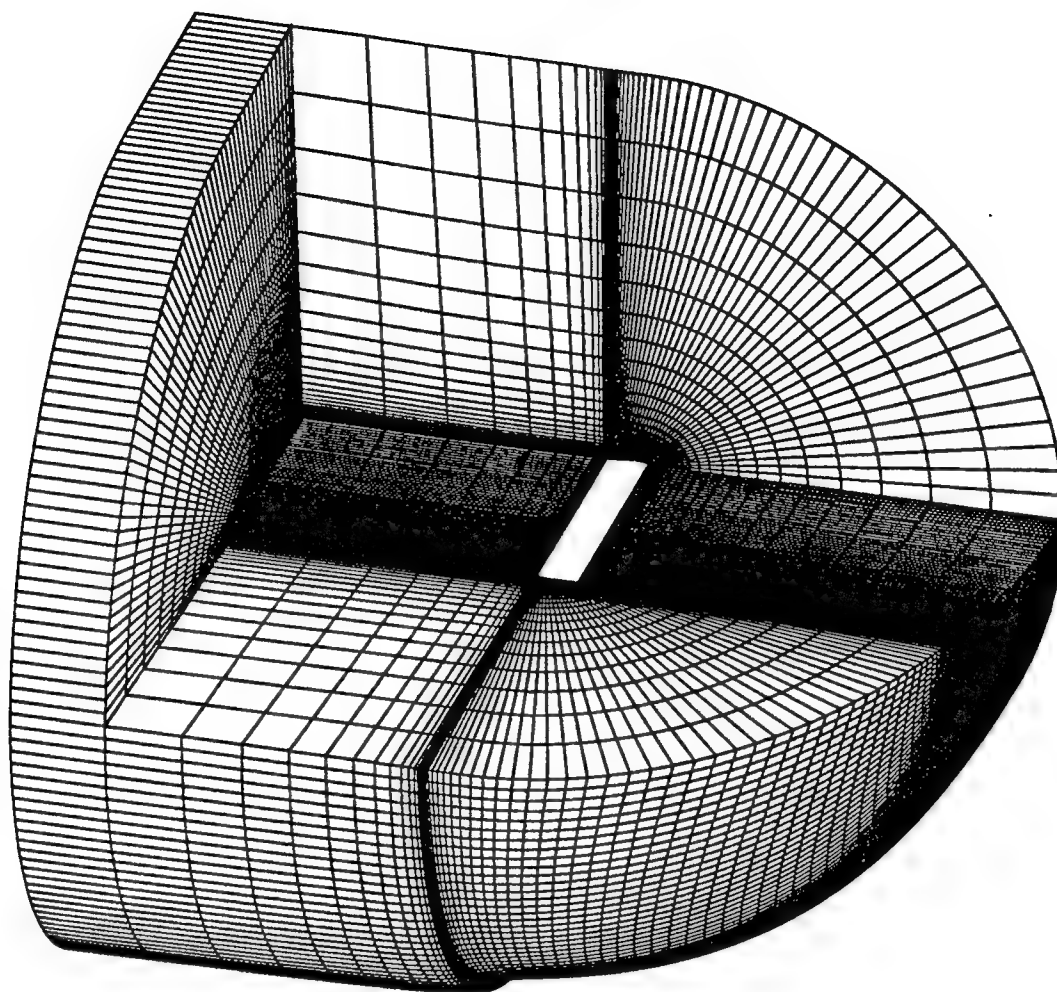
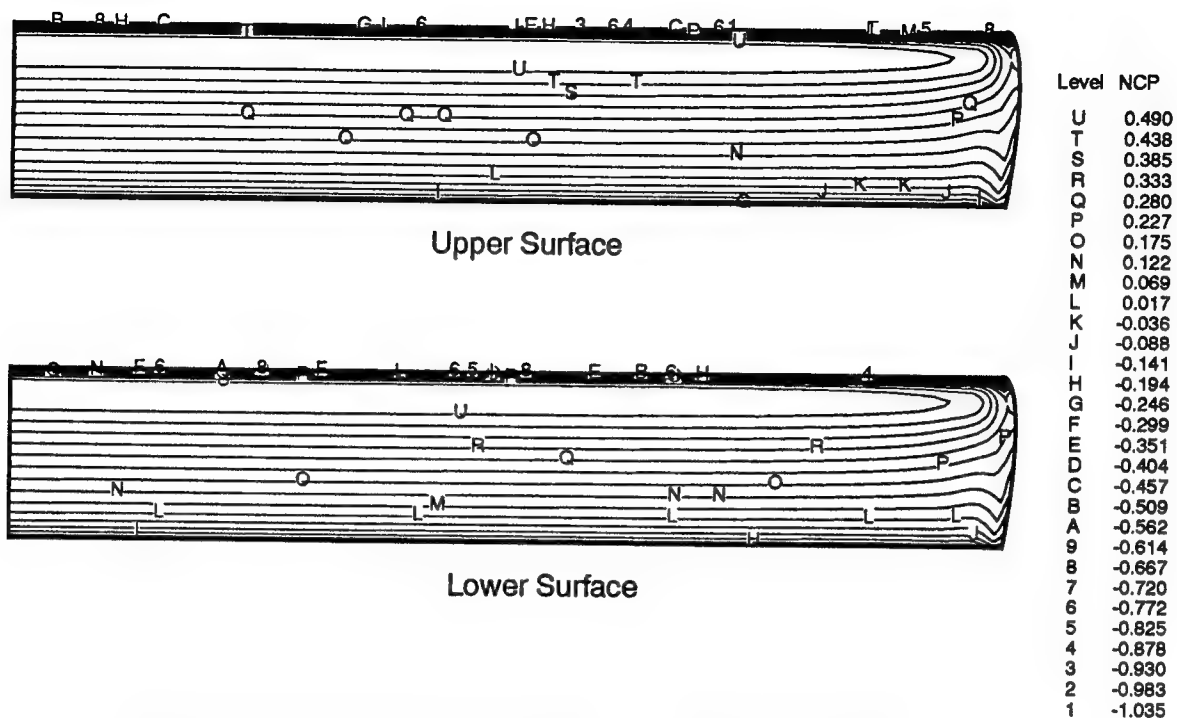


Figure 1. Frames of reference.



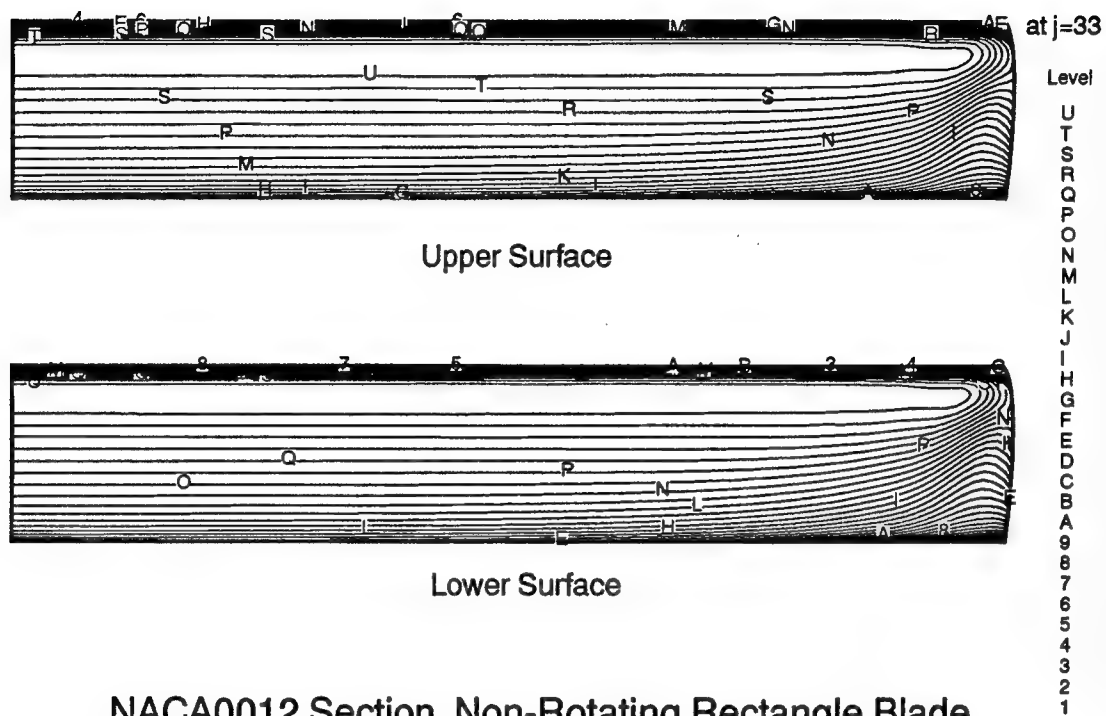
NACA0012 Section, $AR=6$, $\theta=0^\circ$
Partial View of C-O Mesh for Rectangle Blade, 129x65x65 Mesh

Figure 2. C-O mesh.



NACA0012 Section, Non-Rotating Rectangle Blade
 $\theta=\alpha=0^\circ$, $M_\infty=.628$, $R_e=3.7 \times 10^6$, 129x65x65 Mesh
 Calculated Surface Pressure Coefficient Contours

Figure 3a. Non-rotating subsonic flow, pressure coefficient.

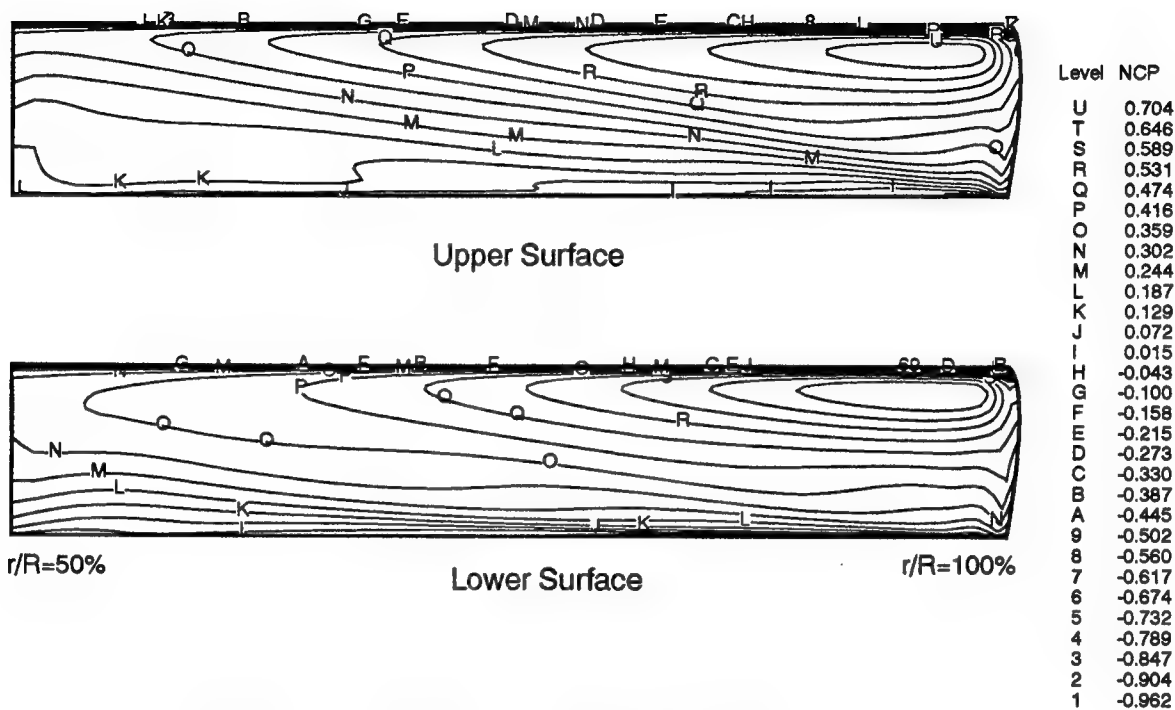


NACA0012 Section, Non-Rotating Rectangle Blade

$\theta=\alpha=0^\circ$, $M_\infty=.628$, $R_e=3.7 \times 10^6$, $129 \times 65 \times 65$ Mesh

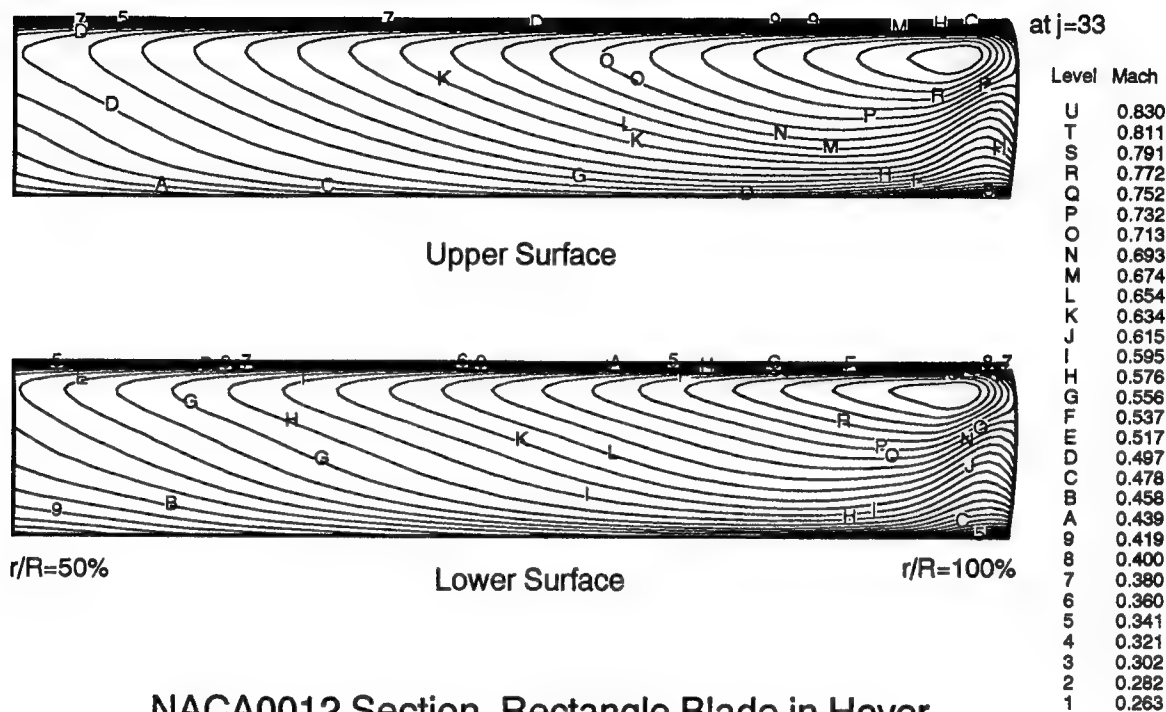
Calculated Local Relative Mach Contours

Figure 3b. Non-rotating subsonic flow, local Mach number.



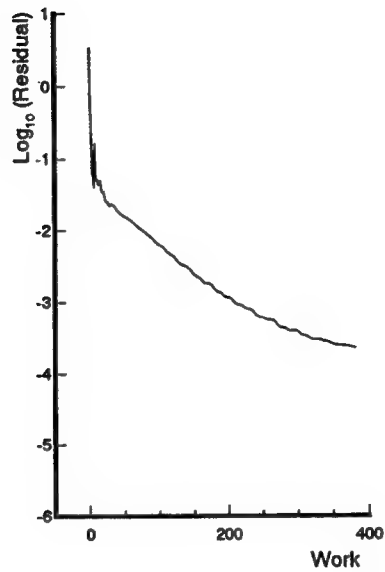
NACA0012 Section, Rectangle Blade in Hover
 $\theta=\alpha=0^\circ$, $M_{tip}=0.628$, $\Omega=0.0619$, $R_e=3.7 \times 10^6$, $129 \times 65 \times 65$ Mesh
 Calculated Surface Pressure Coefficient Contours

Figure 3c. Subsonic flow in hover, pressure coefficient.



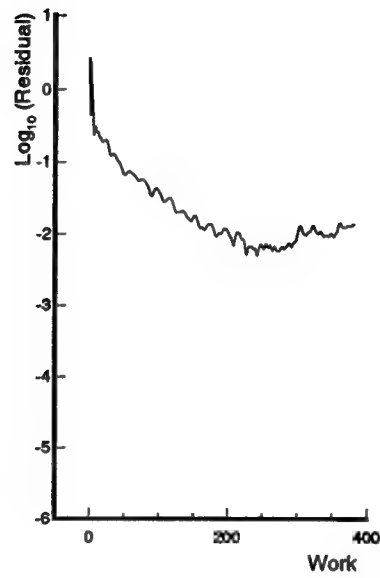
NACA0012 Section, Rectangle Blade in Hover
 $\theta=\alpha=0^\circ$, $M_{tip}=0.628$, $\Omega=0.0619$, $R_e=3.7 \times 10^6$, $129 \times 65 \times 65$ Mesh
 Calculated Local Relative Mach Contours

Figure 3d. Subsonic flow in hover, local Mach number.



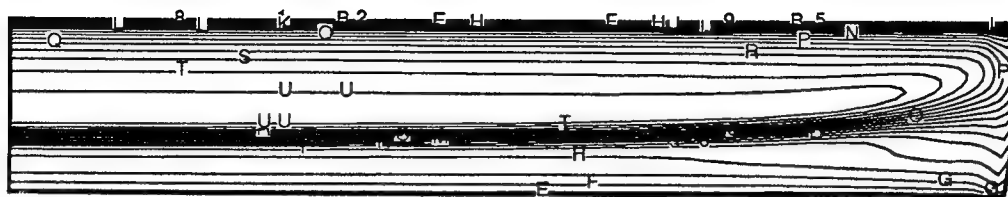
NACA0012 Section, Non-Rotating Rectangle Blade
 $\theta=\alpha=0^\circ$, $M_\infty=.628$, $R_\theta=3.7\times 10^6$, 129x65x65 Mesh
Convergence History in terms of Residual

Figure 3e. Non-rotating subsonic flow, residual.

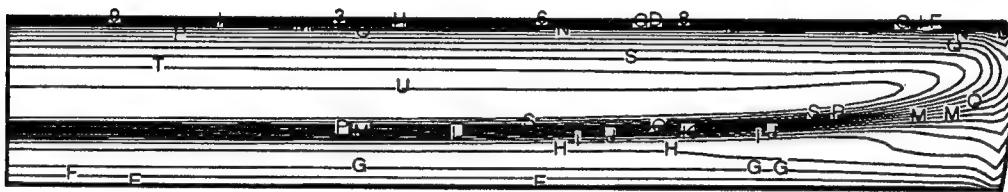


NACA0012 Section, Rectangle Blade in Hover
 $\theta=\alpha=0^\circ$, $M_{tip}=0.628$, $\Omega=0.0619$, $R_e=3.7\times 10^6$, 129x65x65 Mesh
Convergence History in terms of Residual

Figure 3f. Subsonic flow in hover, residual.



Upper Surface

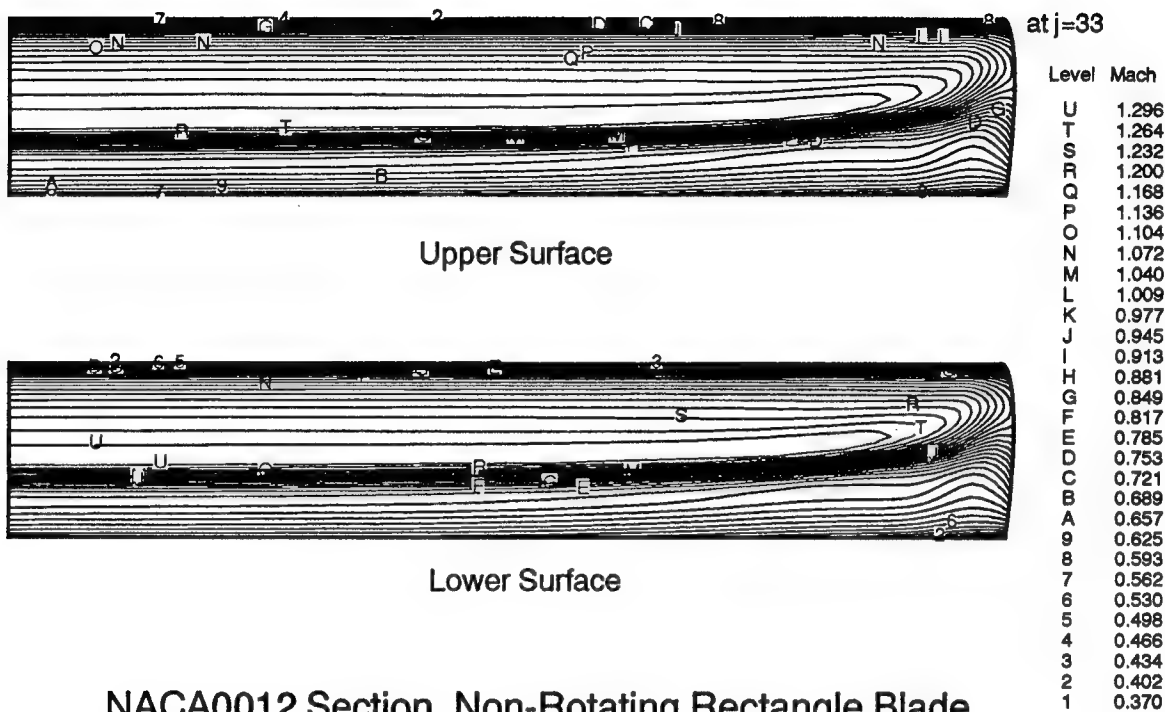


Lower Surface

Level	NCP
U	0.840
T	0.772
S	0.705
R	0.637
Q	0.570
P	0.502
O	0.435
N	0.367
M	0.300
L	0.232
K	0.165
J	0.097
I	0.030
H	-0.038
G	-0.105
F	-0.173
E	-0.240
D	-0.308
C	-0.375
B	-0.443
A	-0.510
9	-0.578
8	-0.645
7	-0.713
6	-0.780
5	-0.848
4	-0.915
3	-0.983
2	-1.050
1	-1.118

NACA0012 Section, Non-Rotating Rectangle Blade
 $\theta=\alpha=0^\circ$, $M_\infty=.84$, $R_e=4.97 \times 10^6$, 129x65x65 Mesh
 Calculated Surface Pressure Coefficient Contours

Figure 4a. Non-rotating transonic flow, pressure coefficient.

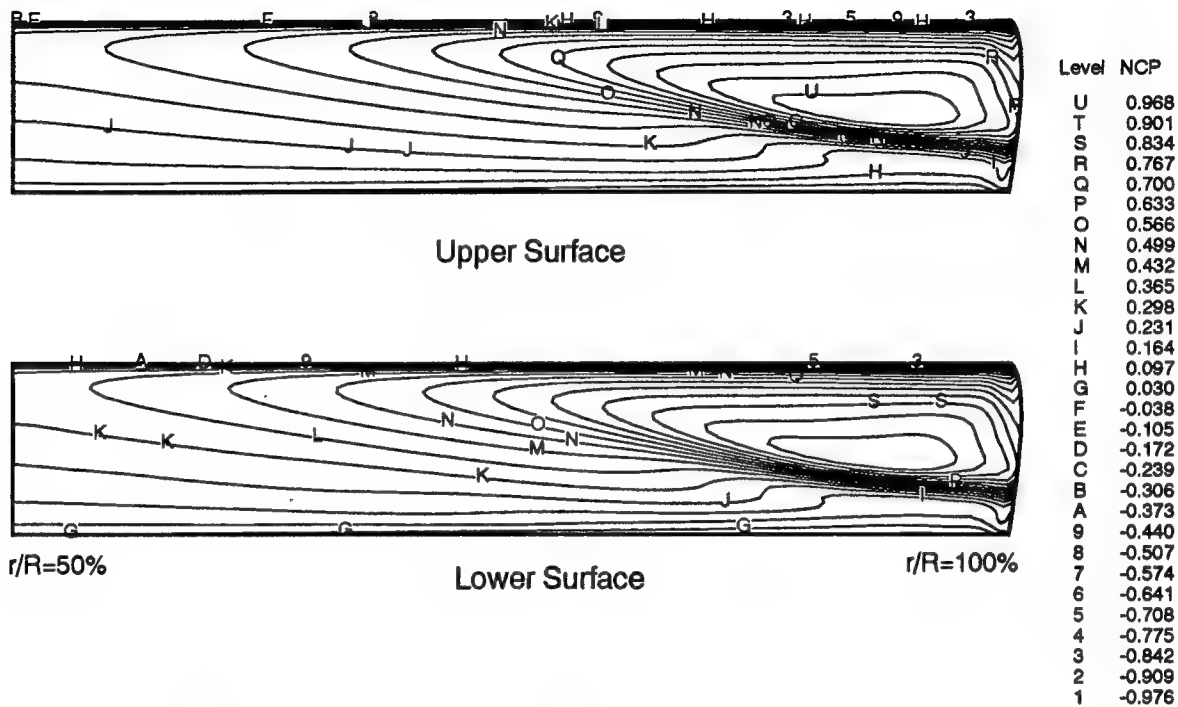


NACA0012 Section, Non-Rotating Rectangle Blade

$\theta=\alpha=0^\circ$, $M_\infty=.84$, $R_e=4.97 \times 10^6$, $129 \times 65 \times 65$ Mesh

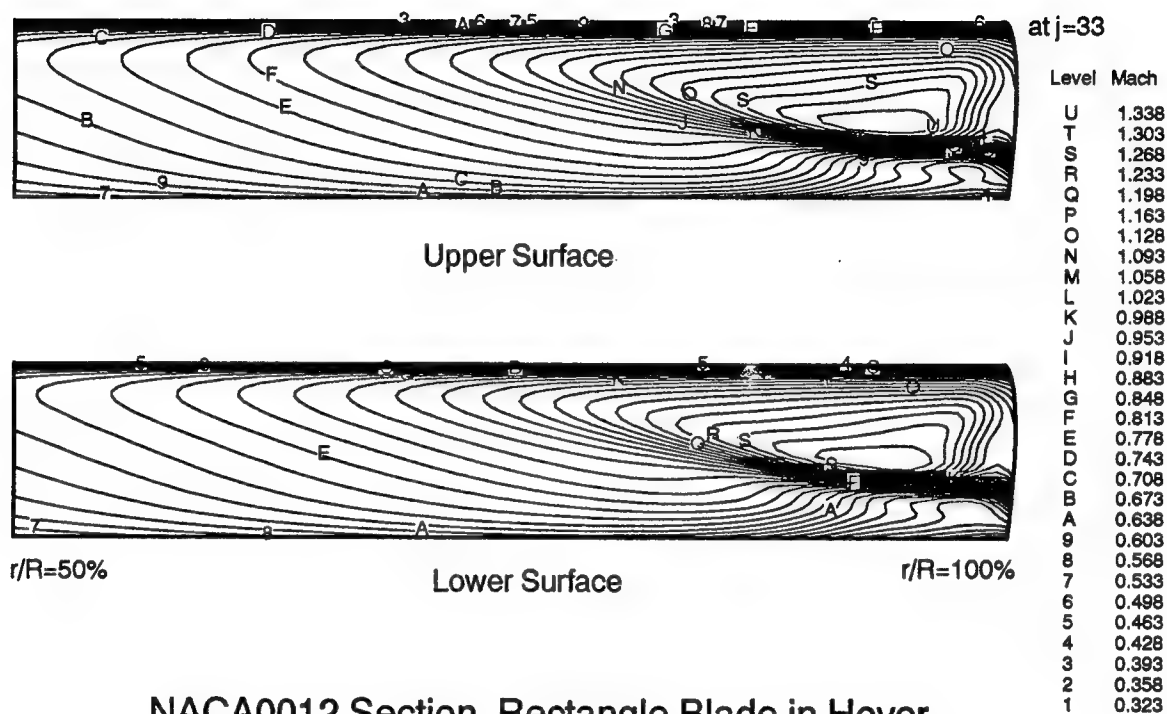
Calculated Local Relative Mach Contours

Figure 4b. Non-rotating transonic flow, local Mach number.



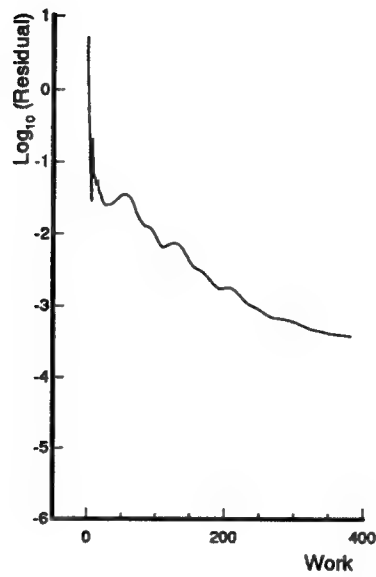
NACA0012 Section, Rectangle Blade in Hover
 $\theta=\alpha=0^\circ$, $M_{tip}=0.84$, $\Omega=0.0828$, $R_e=4.97 \times 10^6$, $129 \times 65 \times 65$ Mesh
 Calculated Surface Pressure Coefficient Contours

Figure 4c. Transonic flow in hover, pressure coefficient.



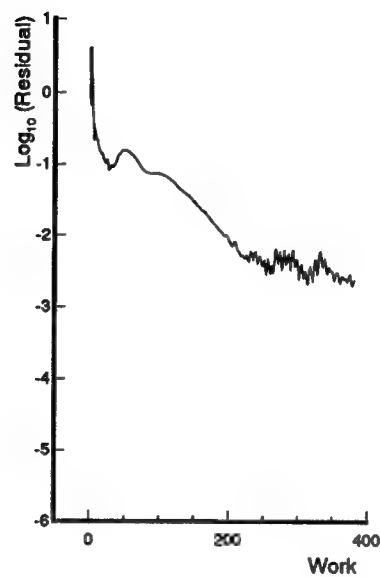
NACA0012 Section, Rectangle Blade in Hover
 $\theta=\alpha=0^\circ$, $M_{tip}=0.84$, $\Omega=0.0828$, $R_e=4.97 \times 10^6$, 129x65x65 Mesh
 Calculated Local Relative Mach Contours

Figure 4d. Transonic flow in hover, local Mach number.



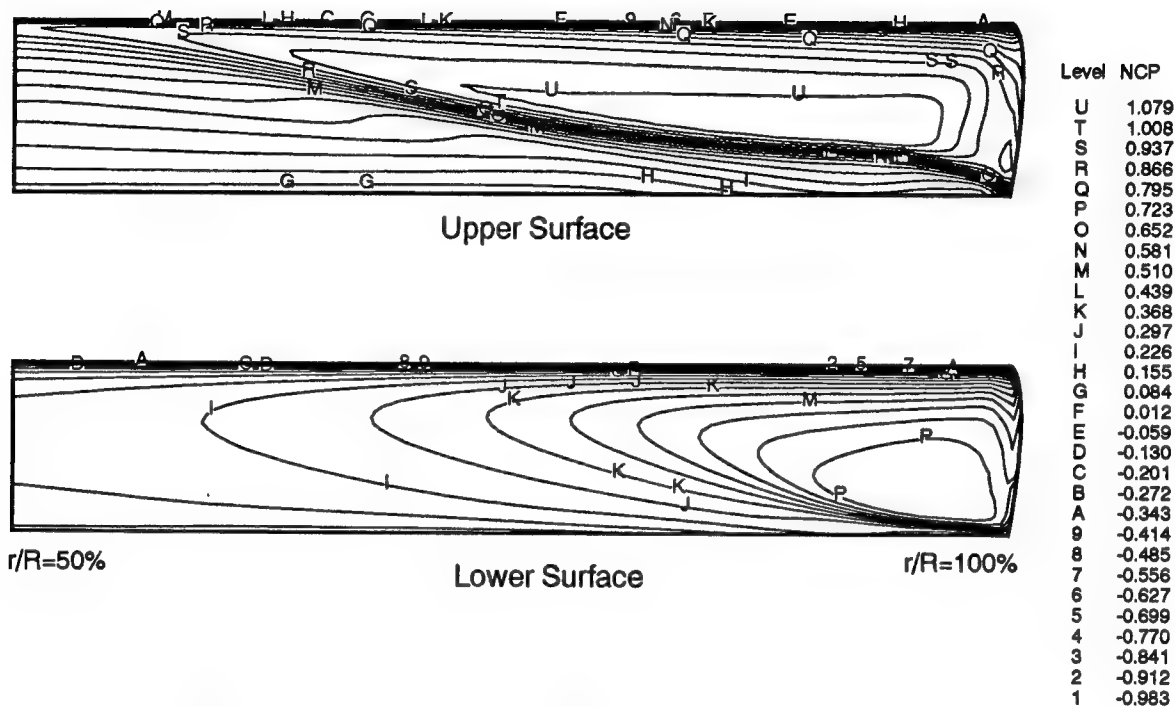
NACA0012 Section, Non-Rotating Rectangle Blade
 $\theta=\alpha=0^\circ$, $M_\infty=.84$, $R_\delta=4.97\times 10^6$, 129x65x65 Mesh
Convergence History in terms of Residual

Figure 4e. Non-rotating transonic flow, residual.



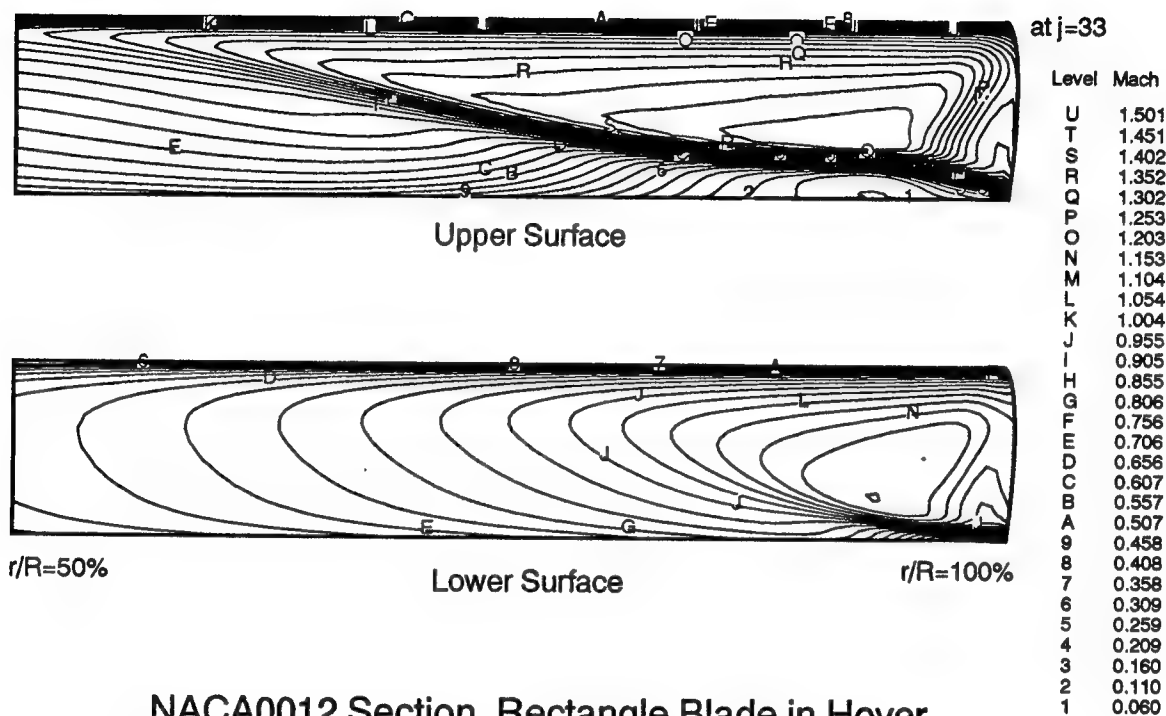
NACA0012 Section, Rectangle Blade in Hover
 $\theta=\alpha=0^\circ$, $M_{tip}=0.84$, $\Omega=0.0828$, $R_e=4.97 \times 10^6$, 129x65x65 Mesh
 Convergence History in terms of Residual

Figure 4f. Transonic flow in hover, residual.



NACA0012 Section, Rectangle Blade in Hover
 $\theta=\alpha=4.2^\circ$, $M_{tip}=0.877$, $\Omega=0.0865$, $R_e=3.93 \times 10^6$, 129x65x65 Mesh
 Calculated Surface Pressure Coefficient Contours

Figure 5a. Lifting transonic flow in hover, pressure coefficient.



NACA0012 Section, Rectangle Blade in Hover
 $\theta=\alpha=4.2^\circ$, $M_{tip}=0.877$, $\Omega=0.0865$, $R_e=3.93 \times 10^6$, $129 \times 65 \times 65$ Mesh
 Calculated Local Relative Mach Contours

Figure 5b. Lifting transonic flow in hover, local Mach number.

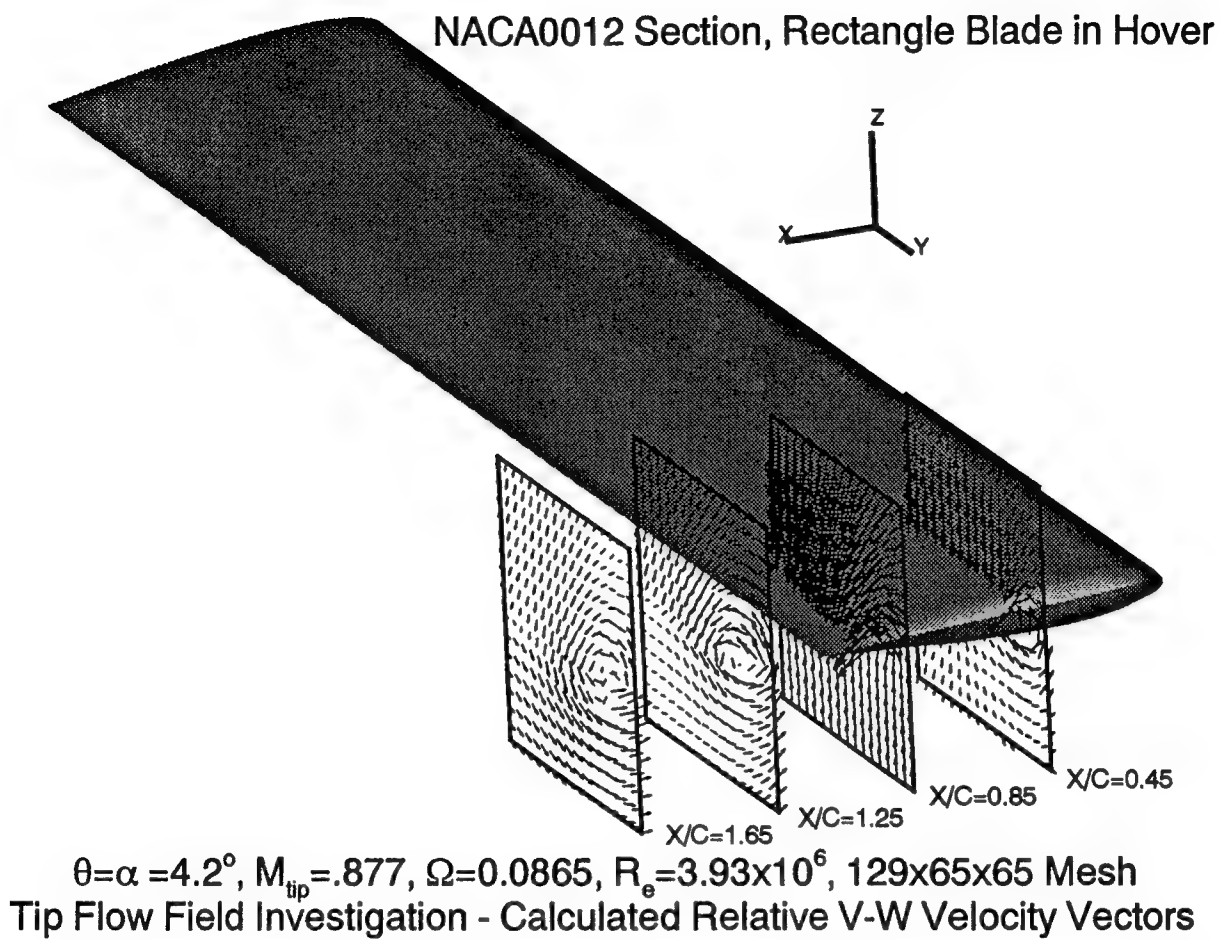
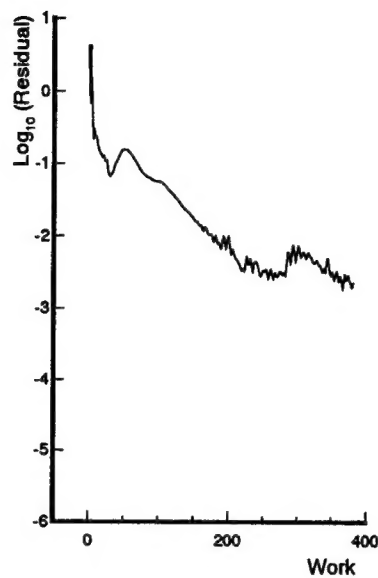


Figure 5c. Lifting transonic flow in hover, tip flow field investigation.



NACA0012 Section, Rectangle Blade in Hover
 $\theta=\alpha=4.2^\circ$, $M_{tip}=0.877$, $\Omega=0.0865$, $R_e=3.93 \times 10^6$, 129x65x65 Mesh
 Convergence History in terms of Residual

Figure 5d. Lifting transonic flow in hover, residual.

LIST OF PUBLICATIONS

None.

LIST OF PARTICIPATING SCIENTIFIC PERSONNEL

1. Hong Hu, Principal Investigator, Associate Professor, Department of Mathematics, Hampton University.
2. Terry G. Logan, Graduate Student, Department of Mathematics, Hampton University, Degree Earned: Master of Science in Applied Mathematics, (the M.S. Thesis was supported by the NASA Grant NAG-1-1170).
3. George H.C. Page, Jr., Graduate Student, Department of Mathematics, Hampton University.

LIST OF INVENTIONS

None.